Modeling the Dynamic Global Distribution of the Ring Current Oxygen Ions Using Artificial Neural Network Technique

Qiushuo Wang[1], Chao Yue [1], Jinxing Li[2], Jacob Bortnik[2], Donglai Ma[2], Chae-Woo Jun[3s]

[1] Institute of Space Physics and Applied Technology, Peking University, Beijing, China

[2] Department of Atmospheric and Oceanic Sciences, UCLA, Los Angeles, CA, USA.

[3] Institute for Space-Earth Environmental Research (ISEE), Nagoya University, Nagoya, Japan

Corresponding author: Chao Yue (yuechao@pku.edu.cn)

Key Points:

- An artificial neural network model was built to reconstruct ring current oxygen ions using geomagnetic indices as input.
- The model shows high accuracy in out-of-sample tasks and successfully captures the enhancement and decay of oxygen ion fluxes.
- The model successfully reproduces the variation of global distribution for oxygen ions of different energies during geomagnetic storms.

Abstract

The ring current is an important component of the Earth's near-space environment, as its variations are the direct driver of geomagnetic storms that can disrupt power grids, satellite communications, and navigation systems, thereby impacting a wide range of technological and human activities. Oxygen ions (O^+) are one of the major components of the ring current and play a significant role in both the enhancement and depletion of the ring current during geomagnetic storms. Although a standard statistical study can provide average global distributions of ring current ions, it can't offer insight into the short-term dynamic variations of the global distribution. Therefore, we employed the Artificial Neural Network (ANN) technique to construct a global ring current O^+ ion model based on the Van Allen Probes observations. Through optimization of the combination of input geomagnetic indices and their respective time history lengths, the model can well reproduce the spatiotemporal variation of the oxygen ion flux distributions and demonstrates remarkable accuracy and minimal errors. Additionally, the model effectively reconstructs the temporal variation of ring current O+ ions for an out-of-sample dataset. Furthermore, the model provides a comprehensive and dynamic representation of global ring current O+ ion distribution. It accurately captures the dynamics of O+ ions during a geomagnetic storm with the oxygen ion fluxes enhancement and decay, and reveals distinct characteristics for different energy levels, such as injection from the plasma sheet, outflow from the ionosphere, and magnetic local time asymmetry.

Plain Language Summary

The ring current, a significant part of Earth's space environment, is closely linked to geomagnetic disturbances that can disrupt power grids, satellite communications, and navigation systems, affecting our daily lives. Oxygen ions (O+) are a key component of the ring current during geomagnetic active time. In our study, we use a powerful tool called Artificial Neural Networks (ANN) to create a model for ring current O+ behavior. This model only requires F10.7 and geomagnetic indices as inputs. By carefully selecting the best combination of the geomagnetic indices and their time history, we built a model that can accurately mimic the behavior of oxygen ions observed by satellites. Our model demonstrates that the levels of O+ ion fluxes rise and fall at various locations during geomagnetic disturbance, which is consistent with previous observational trend. The model also helps us to understand the global distribution of O+ ions in real time. During a test case of a geomagnetic storm, the model revealed details about energy-dependent O+ ion flux enhancement and decay.

1 Introduction

The terrestrial ring current is a distinctive current system flowing toroidally around the Earth, centered at the equatorial plane over a geocentric distance ranging from $\boldsymbol{L \sim 2}$ to $\boldsymbol{L \sim 7}$. Here the McIlwain $\boldsymbol{L}$ is the distance in Earth radii ($\boldsymbol{R_E}$) from the Earth's center to the point where a geomagnetic field line crosses the equator (Daglis et al., 1999). The enhancement of ring current causes global decreases in the Earth's surface magnetic field, known as geomagnetic storms. Intense geomagnetic storms can disrupt power grids, satellite communications, and navigation systems, impacting various technological and human activities. The ring current is formed due to the collective azimuthal drift of energetic charged particles due to the gradient and curvature of

the Earth's magnetic field (Baumjohann & Treumann, 1996). Electrons move eastward, while energetic ions above a several keV typically move westward (De Michelis et al., 1997; Yue et al., 2017), forming the westward directed ring current.

The ring current is mainly composed of hydrogen (H+), helium (He+) and oxygen (O+) ions from ~10s to several hundreds of keV (Williams, 1987; Daglis et al., 1993; Fu et al., 2023). Due to the negligible mass (and hence energy density) of electrons, their contribution to the ring current is minor (Baumjohann, 1993). During quiet times, H+ is the dominant ion species, while the contribution from O+ increases drastically during active times and may become the dominant ion species during the storm main phase (e.g. Daglis et al., 1999; Yue et al., 2019). Daglis (1997) showed that as the storm intensity increases, the contribution of O+ to the ring current rises. Yue et al. (2019) showed that the O+ ion fluxes intensify during the storm main phase and then rapidly decay during the storm recovery phase, suggesting that O+ ion buildup and decay rates are significantly faster than H+ ions. The faster build-up is probably related to some species-dependent source and/or energization processes in the inner magnetosphere (e.g., Yue et al., 2019), while the faster decay of O+ ions may be caused by the faster charge exchange and Coulomb collision rates (e.g., Chen et al., 2020).

Ring current ions may originate from the Earth's plasma sheet and/or directly enter the inner magnetosphere from the terrestrial ionosphere (e.g. Chappell et al., 1987, 2000, 2008; Delcourt et al., 1992; Gkioulidou et al., 2019; Huddleston et al., 2005; Keika et al., 2016, 2018; Kronberg et al., 2014; Sheldon et al., 1998; Yue et al., 2020). With increasing geomagnetic activity, a broader range of ion species, including the heavy O+ ions, are transported into the inner magnetosphere, thereby enhancing the ring current. During this transport process, these ions gain energy through adiabatic transport driven by large-scale convection, mesoscale impulsive dipolarizations, and localized nonadiabatic acceleration (Keika et al., 2013; Yang et al., 2011; Zong et al., 2012; Zhou et al., 2012). During geomagnetically active periods, ring current ions including O+ ions, are depleted due to Coulomb collisions and charge exchange processes with the geocorona, as well as pitch-angle scattering induced by electromagnetic ion cyclotron (EMIC) waves (Jordanova et al., 1997; Jordanova, 2007; Kennel & Petschek, 1966; Meredith et al., 2003) and current sheet scattering (Donovan et al., 2003; Liang et al., 2014; Sergeev & Tsyganenko, 1982; Sergeev 87 et al., 1983, 1993; Yue et al., 2014). These mechanisms lead to the decay of the ring current back to quiescent levels.

The Artificial neural network (ANN) model has become a powerful machine learning (ML) technique able to build empirical models with the development of hardware facilities and the increasing computing power in recent years. Recent studies (e.g. Chu et al., 2021) show that ANN model for radiation belt electrons does not rely on any initial conditions, boundary conditions, or certain assumptions. Compared with traditional empirical models (e.g. Claudepierre et al., 2016), the ANN model offers a remarkable advantage in capturing intricate patterns and relationships directly from data that are very hard to detect otherwise. This is particularly advantageous when dealing with complex, nonlinear systems or when the underlying physics is not well understood. Moreover, ANN excels at handling noisy or incomplete data, making them a robust choice for space science scenarios where data quality from satellites may vary. Additionally, their scalability to large and high-dimensional datasets further enhances their utility in various domains. Utilizing the ANN technique, Bortnik et al. (2016) developed a method to use ANNs to capture the spatiotemporal variability of plasma density at the equatorial

region, employing the Sym-H index as the primary predictor. Chu, Bortnik, Li, Ma, Denton, et al. (2017); Chu, Bortnik, Li, Ma, Angelopoulos, and Thorne (2017) and Zhelavskaya et al. (2017) created dynamic plasma density models using multiple input sources, including solar wind parameters in addition to time series of geomagnetic indices. Additionally, the ANN technique has proven successful in reconstructing distributions of radiation belt electrons (S. G. Claudepierre & O'Brien, 2020; Chu et al., 2021; Ma et al., 2022; Landis et al., 2022) and wave distributions (Bortnik et al., 2018; Guo et al., 2022). Li et al. (2023) developed an ANN model to reconstruct the distribution and dynamic variation of ring current protons by optimizing the best combination of geomagnetic indices and time history length.

In this study, we utilize the ANN model to predict ring current oxygen ion fluxes across a range of energy channels spanning from 38 keV to 870 keV. The ANN model is constructed based on particle fluxes measured aboard the Van Allen Probes, and uses solely geomagnetic indices as input parameters. Notably, the ANN model operates independently of any specific initial or boundary conditions, relying instead on the direct influence of geomagnetic activity, as expressed by the geomagnetic indices on the fluctuations in ring current oxygen ion fluxes. This unique characteristic, which distinguishes the ANN model from traditional physics-based approaches, opens up new avenues for comprehending the dynamics of the ring current. Furthermore, our ANN model exhibits exceptional robustness, effectively filtering out noise presented in the measurements obtained from the Van Allen Probes. This robustness enhances the reliability of our model. Through rigorous analysis, we demonstrate that our ANN model accurately captures the dominant patterns of variability observed during geomagnetic storm periods. Additionally, it accounts for variations across different magnetic local time (MLT) intervals for distinct energy channels, providing valuable insights into the intricate behavior of the ring current under varying conditions.

2 Data Description

The predictors, which are the input parameters of the model, include several geomagnetic and solar indices, the candidate indices are Sym-H, Sym-D, Asy-H, Asy-D, SME, and F10.7. The asymmetric (Asy) and symmetric (Sym) disturbance indices describe the geomagnetic disturbances at mid-latitudes, including the horizontal (H) and the east-west (D) components. The 1-min resolution Sym/Asy indices used in this study are obtained from the Coordinated Data Analysis Web (CDAWeb). SME is the SuperMAG version of Auroral Electrojet (AE) index, which is typically and indication of particle injections during substorms. F10.7 is the solar radio flux at a wavelength of 10.7 cm (2800 MHz), which is an excellent indicator of solar activity and is usually used as a proxy for high frequency X-ray and UV radiation which is strongly attenuated by the atmosphere. Figure 1 illustrates an overview of above mentioned geomagnetic indices and the F10.7 index from 2013 to 2018.

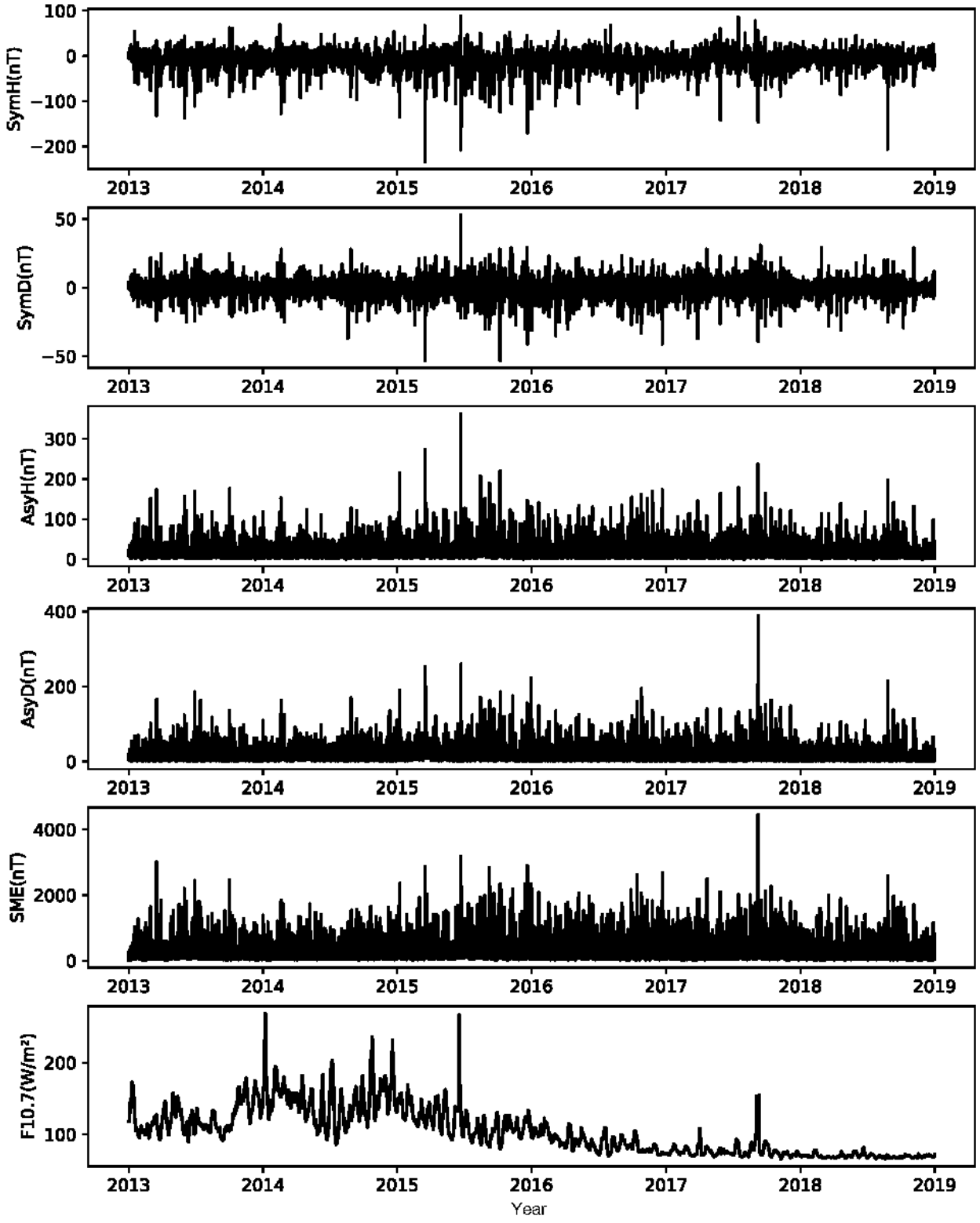

Figure 1. Overview of predictors from 2013 to 2018. The predictors include the (a) Sym-H, (b) Sym-D, (c) Asy-H, (d) Asy-D, (e) SME and (f) F10.7 indices.

The oxygen ion flux data we use in this study are obtained from the Van Allen Probes, which operated on an elliptical orbit of $\mathbf{1.2}\boldsymbol{R_E} \times \mathbf{5.8}\boldsymbol{R_E}$. We use energy channels from $\mathbf{38}\ \boldsymbol{keV}$ to $\mathbf{870}\ \boldsymbol{keV}$, with data from $\mathbf{38-52}\ \boldsymbol{keV}$ measured by the Helium Oxygen Proton Electron (HOPE) instrument (Funsten et al., 2013), and data from $\mathbf{71-870}\ \boldsymbol{keV}$ measured by the Radiation Belt Storm Probes Ion Composition Experiment (RBSPICE) instrument (Mitchell et al., 2013). Data ranges from February 2013 to April 2019, and is reduced to have a time resolution of 1 minute. Figure 2 shows O+ ion fluxes at selected energies versus L-shell and the Sym/H, SME, and F10.7 indices throughout 2017.

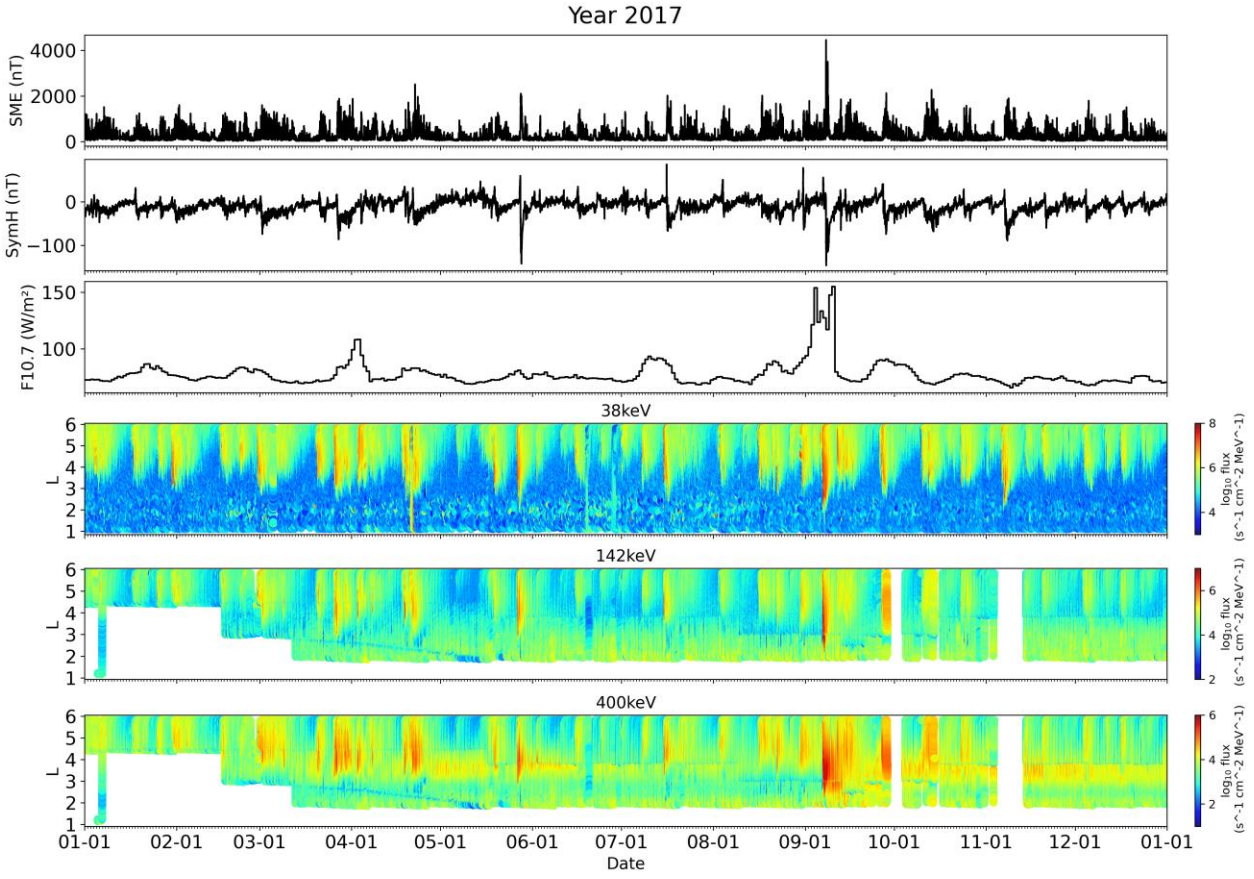

Figure 2. (a) SME, (b) Sym-H, (c) F10.7, and (d-f) oxygen ion fluxes measured throughout the year of 2017.

3 Methodology

3.1 Model Description

In this study, the 2 dimensional (2D) distributions of fluxes of ring current oxygen ions are reconstructed using a fully connected multi-layer ANN. This network consists of massively parallel distributed processors with processing units called neurons. These neurons perform

progressive learning of the inputs using a learning algorithm that involves orderly modification of the synaptic weights until a required objective is achieved as an output.

Each layer in ANN has interconnected neurons, with connections defined by weights matrix $\boldsymbol{W}$ and bias vector $\boldsymbol{b}$. For a given input vector $\boldsymbol{z}$ in layer l, the output of this layer can be expressed as

$$z_j^{l+1} = f\left(\sum_{i=0}^{N-1} z_i^l w_{ij}^l + b_i^l\right)$$

Here, i and j are the number of neurons in each layer, w_{ij}^l and b_i^l are the weight and bias in each layer. The activation function $f(z)$ is applied to obtain the final output of the layer. In this study, we use the ReLU function $f(z) = \max(0, z)$, which is widely used for regression tasks (e.g. Ramachandran et al., 2017). This process is performed at each layer during the forward propagation phase.The output z_j^{l+1} in layer l is the input of the next layer $l + 1$. It allows for the mapping of the input data to nonlinear representations, enabling the network to capture complex patterns and relationships. This iterative process continues until it reaches the output layer.

In the training process, the ANN model can adjust the weights (w_{ij}^l) and biases (b_i^l) of each layer automatically (Rumelhart et al., 1986), minimizing the difference between the network's final output and the true output (the measured oxygen fluxes). We use Tensorflow software, adopting 2 hidden layers and 75 neurons for each layer. We choose mean square error (MSE) as the loss function and use stochastic gradient descent (SGD) optimizer to minimize it. The training process stops when the training goes for 2000 epoches or the MSE of the validation set stops improving for 32 consecutive steps to prevent overfitting (Ma et al., 2022). The model performance is evaluated in term of the coefficient of determination R of the test set, which is expressed as

$$R = \sqrt{1 - \frac{\sum_i (z_i - \hat{z})^2}{\sum_i (z_i - \bar{z})^2}}$$

Here z_i is the measured value for each test sample, $\bar{z}$ is the mean value of z_i, and $\hat{z}$ is the predicted value for each test sample.

Since the particle flux span over a few orders of magnitude, we model the lograrithm of the particle flux with a base of 10, and remove all invalid flux data. The whole data set are split into contiguous 1-day segments (Ma et al., 2022; Li et al., 2023). We first we use a 5-fold cross-validation method to find out the best combination of input parameters. We select each whole year as the test set, and partition the rest of data segments into a training set ($\sim 80\%$) and a validation set ($\sim 20\%$). After we obtain the optimal combination of predictors, we construct a new model using the predictors that produce the best performance.

3.2 Selection of input parameters and time history length

The input to the first layer in our model includes $X(t_0)$ and $P(t_0)$. $X(t_0)$ is the spacecraft's location in the solar magnetospheric (SM) coordinates at the time of the observation t_0, including $L, cos\theta, sin\theta, MLAT$. Here $MLAT$ is the geomagnetic latitude, θ is the azimuthal angle where 0° indicates the direction pointing to the Sun. We use both $cos\theta$ and the $sin\theta$ to describe the azimuthal coordinate is to eliminate the discontinuity at $\theta = 0$ following the approach of Bortnik et al. (2016). $P(t_0)$ is a $m \times n$ tensor denoting a series of geomagnetic indices, where m denotes the number of geomagnetic indices used, and n denotes the time history length with with a 1-hour resolution. Specifically, the number P_{ij} denotes the *i*th predicter at the time of *j* hours prior to t_0.

Following the procedure of the work by Ma et al., (2022), we perform a series of experiments to select the optimal predictors. We first use coordinates as the only input, and perform 5 experiments in which each whole year of data is used as the test set. Then we calculate the averaged R score. Table 1 illustrates the results for the 52 keV O+ ions, showing an averaged R score of 0.434. Then, we add each candidate parameter (including their history over the past few days) into the input., and evaluate the resultant R score. The model incorporating the SME index produce a R score of 0.743, outperforming those incorporating other parameters. We continue this process, and identify the parameters that most efficiently improve our model. The exploration for optimal predictors concludes when the model ceases to yield improvements when adding additional parameters.

The SME index makes the most significant improvement to the model performance, increasing the R value of 52 keV O+ from 0.43 to 0.74. This possibly reflects that substorm effects make a major contribution to the ring current O+ ion enhancements. Table 1 suggests that the combination of SME + Sym-H + F10.7 yields the best performance for modeling the 52 keV O+ ion flux. This is understandable, since the Sym-H index reflects the intensity of the ring current iteself, the SME reflects the intensity of substorm injections, and the F10.7 reflects the intensity of solar illumination which closely correlates with the degree of photoionization in the ionosphere and potential upflow/outflow of the O+ ions. All these activities can direct impact the sources of ring current oxygen ions.

Input parameters		**R score**
Settled parameters	**Pending parameters**	
	Coordinates	0.434
coordinates	Sym-H	0.478
	Sym-D	0.460
	Asy-H	0.451
	Asy-D	0.429
	SME	0.743
	F10.7	0.387
coordinates + SME	Sym-H	0.832
	Sym-D	0.824
	Asy-H	0.831
	Asy-D	0.824
	F10.7	0.828
coordinates+ SME + sym-H	Sym-D	0.830
	Asy-H	0.839
	Asy-D	0.828
	F10.7	0.846

coordinates+ SME + sym-H + F10.7	Sym-D	0.834
	Asy-H	0.835
	Asy-D	0.82

Table 1: The process to find the best input parameter combinations for 52 keV oxygen ions fluxes model. The cells highlighted by green color are the highest R score for each step, and the cell highlighted as yellow is the highest R score in the training process, which indicates the best combination of input parameters for 52 keV oxygen ion fluxes.

We repeated the input-parameter-optimizing technique on other energy channels, and find that the combination of SME + Sym-H + F10.7 roughly produce the best model performance across all energies. Therefore, we adopt these parameters in the model for all energies from 38 keV to 870 keV.

Since the O+ lifetime varies over different energies (and different L-shells), we select the optimal history length for the O+ modeling of different energies. An overly short history length will result in an underfitting model that lacks sufficient information about past events, while a overly long history length will result in an overfitting as the model collects too much information that does not contain the relevant information. We try to change the different history length ranging from 0 to 10 days with a resolution of 1-day for the model. We split the segments into ~ 70% training set, ~ 15% validation set and ~ 15% test set to optimize the best history length. The best time history lengths for 38 and 142 keV were both found to be 5 days, and for 400 keV channel was found to be 2 days which stands in contrast to the electron energy channels that typically require longer time histories for larger energies (Ma et al., 2022, Chu et al., 2021).

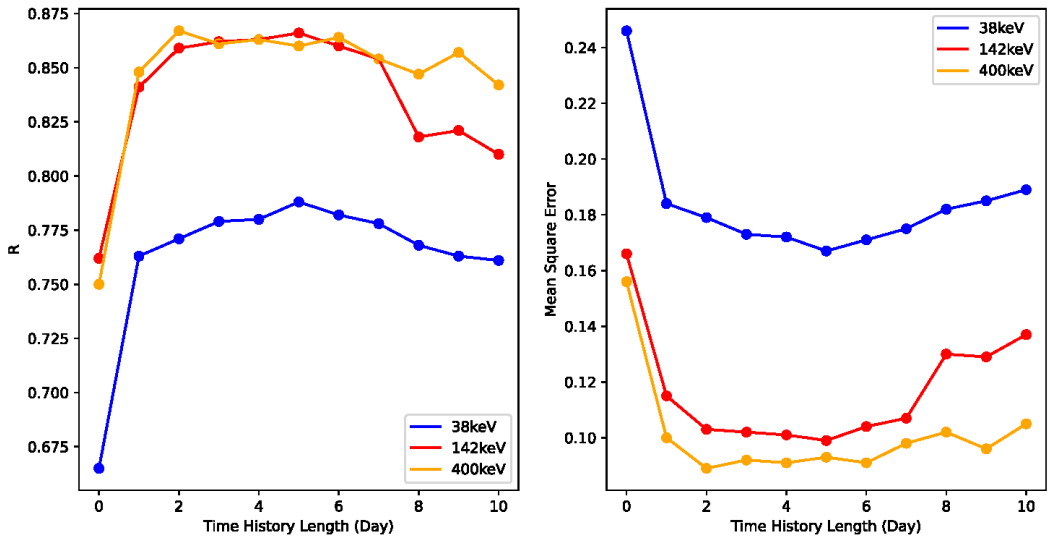

Figure 3: R score (left panel) and mean square error (right panel) of ANN models of the O+ fluxes for the test data set as a function of history lengths for selected energies.

4 Model Results

We build our ANN models by adopting the optimized combination of input parameters and history length, and hold out the data in 2017 as test set to illustrate the model's out-of-sample performance over long term. Note that the year 2017 observed low solar activity but multiple strong geomagnetic storms. Figure 4 shows the out-of-sample performance of the three selected energies by comparing the log_{10} of the measured fluxes versus log_{10} of the model fluxes in a two-dimensional distribution of occurrence. A perfect regression follows the diagonal red solid line (y = x) and yields R = 1 between the observations and model results. Our model results indicate that the ANN models can predict the (sequentially organized) out-of-sample ring current O+ fluxes with more than **70**% accuracy which is the most accurate global model of O+ ion fluxes at the present time, to the best of our knowledge.

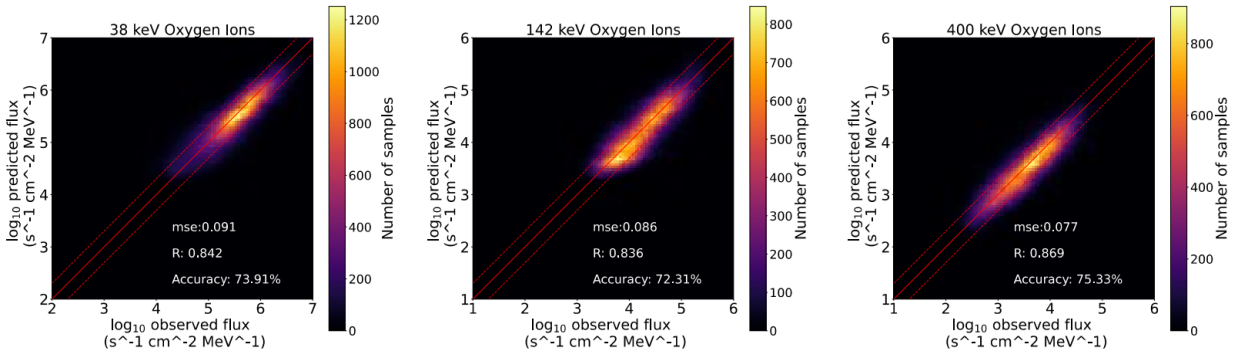

Figure 4: Model performance on the test data set for O+ fluxes at energies of (a) 38, (b) 142, and (c) 400 keV.

Figure 5 provides a comparative analysis between the measured 38 keV O+ fluxes and the ANN modeled results over the whole year of 2017 which has not been involved in the model training and is fully out of sample, as noted above. Figures 5a-5c show the variations of SME, Sym-H and F10.7 indices which serve as inputs to the model. It could be seen from Sym-H index that there are several large geomagnetic storms with minimum SYM-H index less than -100 nT. Figure 5d shows the measured 38 keV O+ flux as a function of L-shell and time along Van Allen Probe B's orbit. The modeled O+ flux, shown in Figure 5e, captures the rapid intensification and subsequent decay during geomagnetic storms in a realistic way. Notably, the discrepancy between the model predictions and the measured data are generally minimal, as depicted in Figure 5f with the largest relative errors typically occurring when the observed fluxes become very low (e.g., at L<3), which are also the times when the ring current plays the smallest role in space weather effects.

Figure 6 shows the model performance for 142 keV O+ fluxes in a similar format to Figure 5. The behavior of 142 keV oxygen ions is different from that of 38 keV: the magnitude of flux variations is smaller than that of 38 keV oxygen ions, and it is seen that the model successfully captures these characteristics. In addition, it should be noted that Figure 6 demonstrates the robustness of our model: RBSPICE exhibits a continuous period of noisy data from mid-March to mid-May at $\boldsymbol{L = 2.5}$, as shown in Figure 6d. Remarkably, the model adeptly filters out the noise present in the original data (Figure 6f), underscoring its reliability.

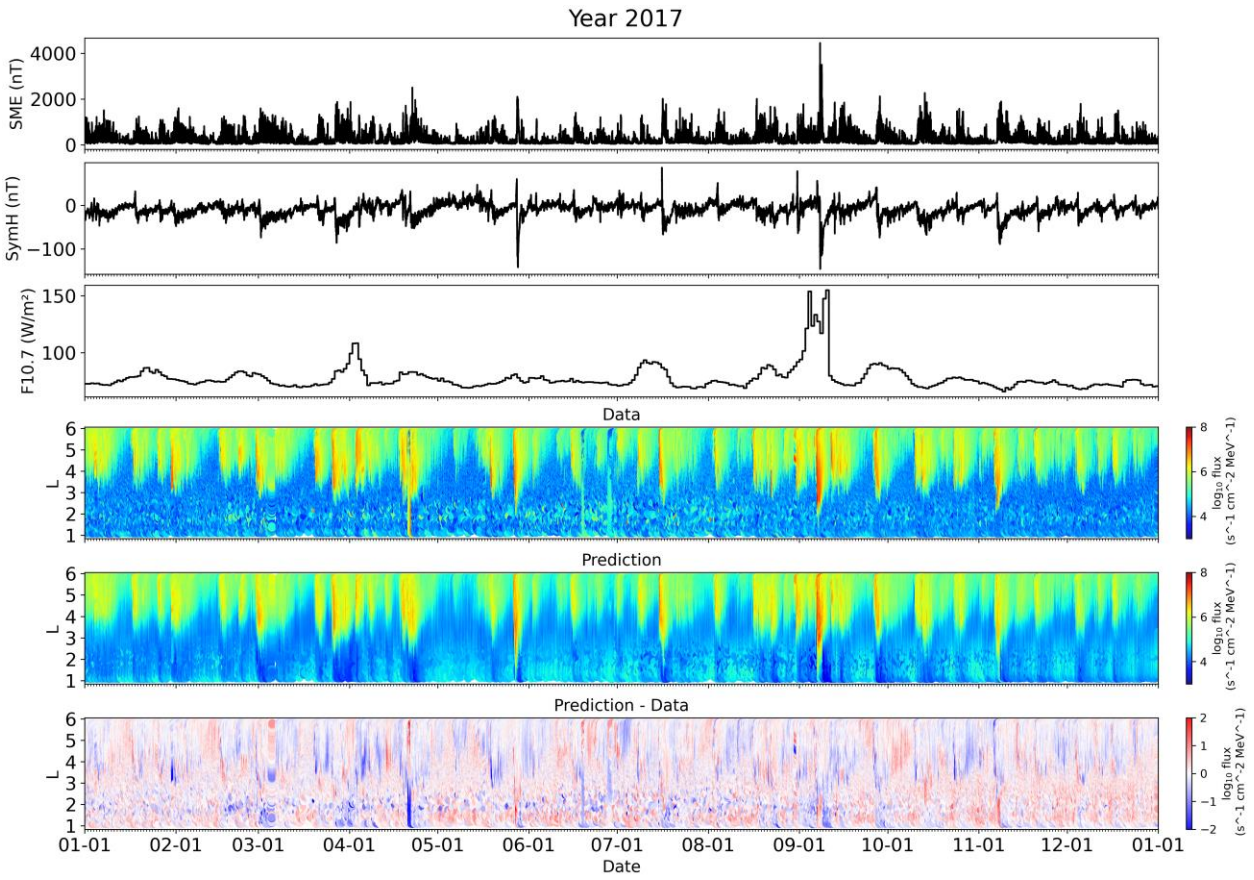

278

279 **Figure 5: Comparison between measured fluxes and modeled fluxes for 38 keV through the**
280 **year 2017. (a) SME value. (b) Sym-H value. (c) F10.7 value. (d) The log_{10} observed 38 keV**
281 **O+ fluxes measured by Van Allen Probe B. (e) The log_{10} modeled 38 keV O+ fluxes. (f) the**
282 **log_{10} modeled fluxes minus log_{10} observed fluxes.**

283

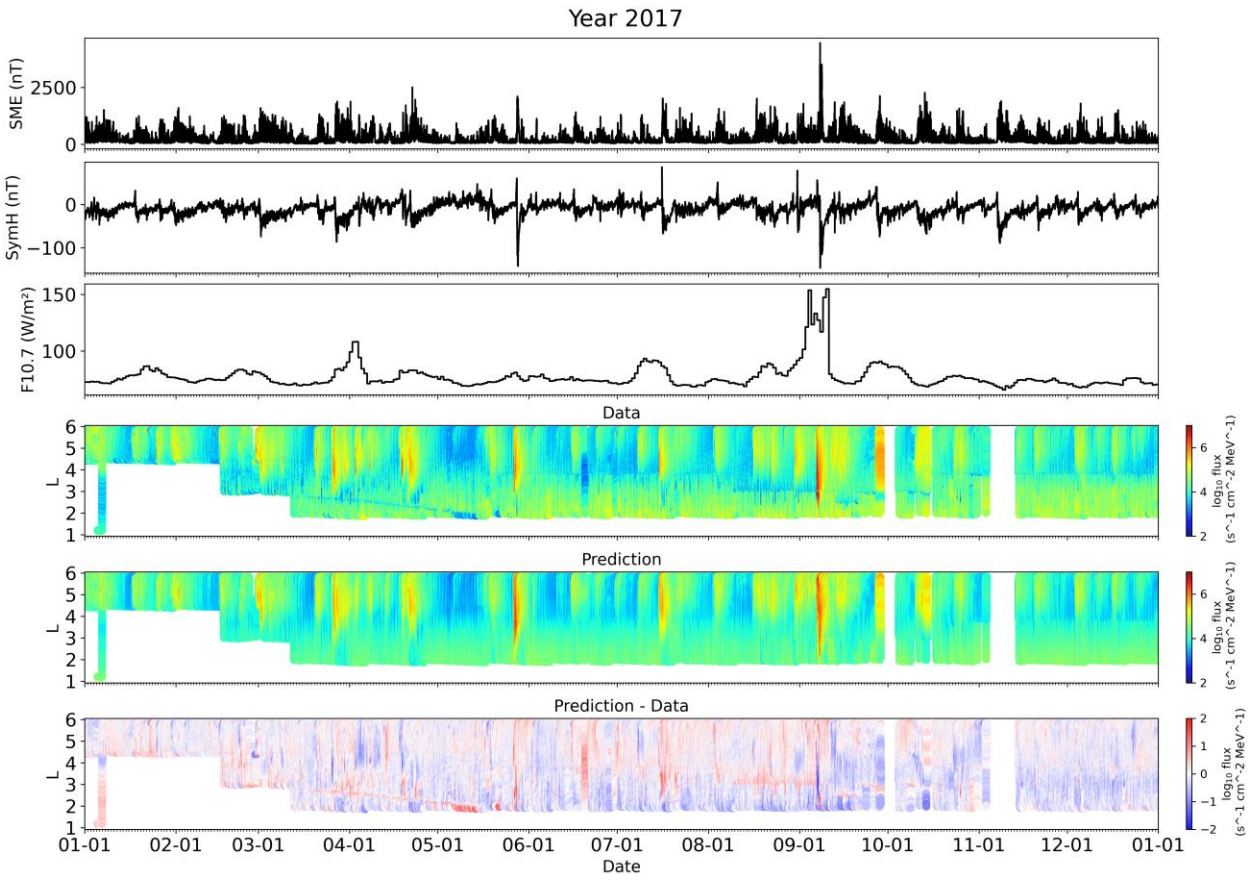

Figure 6: Same format as Figure 5 but for 142 keV O+ fluxes.

ANN models have the advantage that they are capable of reconstructing the global distribution of ring current oxygen ions (based directly on the data itself), whereas satellites only provide single-point observations. This holds significant implications for our understanding of the O+ enhancement and loss during storm events. Figure 7 illustrates the modeled global distribution of 38, 142 and 400 keV O+ fluxes during a large geomagnetic storm spanning from 27 May to 30 May 2017. Figures 7a and 7b show the variation of Sym-H and SME indices during this storm event. Figures 7c-7h illustrates the variation of 38 keV O+ fluxes at six distinct moments representing the pre-storm, the initial main phase, the late main phase, the recovery phase, the subsequent substorm time, and the post-storm time, respectively. During quiet period, the flux level of 38 keV oxygen is small. In the early main phase, a notable asymmetry in the magnetic local time (MLT) is observed, consistent with the physica understanding that enhanced oxygen ions drift is directed toward the pre-midnight to dusk side. This phenomenon arises from oxygen ion injection in the magnetic tail, followed by westward drift induced by magnetic field gradient and curvature. In the late main phase, the model displays symmetry in the dawn-dusk direction due to ring current intensification, while asymmetry is evident in the day-night direction due to continuous plasma sheet injection. During the recovery phase, the flux of 38 keV oxygen ions decreases and the distribution returns to a symmetrical state, with the peak around $\boldsymbol{L = 3-5}$. We reiterate that none of these physical processes have been inserted into the ANN model in any way, it is simply picking up subtle patterns in the data and reconstructing the global O+ distribution according to these patterns.

306 The 142 keV oxygen ions contribute little during quiet time, while during the early main phase,
307 the flux enhance dramatically with strong day-night asysmetry, indicating strong substorm
308 injection as shown in Figure 7b. During the later main phase, these ions penetrate into smaller L
309 shells and move towards dusk side, demonstrating strong dawn-dusk asymmetry. As
310 geomagnetic activity goes down, the flux of 142 keV oxygen ions decreases as shown in Figure
311 7i. When there is another substorm during the recovery phase of geomagnetic storms, the flux of
312 142 keV oxygen ions increases again and it shows fast decay after the storm. The observed
313 asymmetry, peaking on the dusk side during the main phase, recovery phase, and substorm times
314 (Figure 7k-7m), can be understood physically by drift physics in theoretical models (Spence &
315 Kivelson, 1990, 1993), as well as by related findings (Keesee et al., 2011) based on TWINS
316 energetic neutral atom observations.

317 The 400 keV high energy O+ flux exhibit distinct characteristics from low energy O+ fluxes.
318 They do not constitute a substantial part of the storm time ring current due to their low flux
319 levels, as the typical energy range of oxygen ions which contribte the enhancement of the ring
320 current spans from approximately 10 keV to around 100 keV (Fu et al., 2023). Oxygen ions
321 above 100 keV remain stably trapped on the equatorial plane and contribute the quiet time ring
322 current (e.g., Yue et al., 2018). Compared to the 38 and 142 keV O+ fluxes, the 400 keV O+
323 fluxes are more symmetric, possibly because the magnetic drift along closed drift path and their
324 drift periods are short, while the low energy ions are largely impacted by the electric field,
325 leading to an evident asymmetry during storm time.

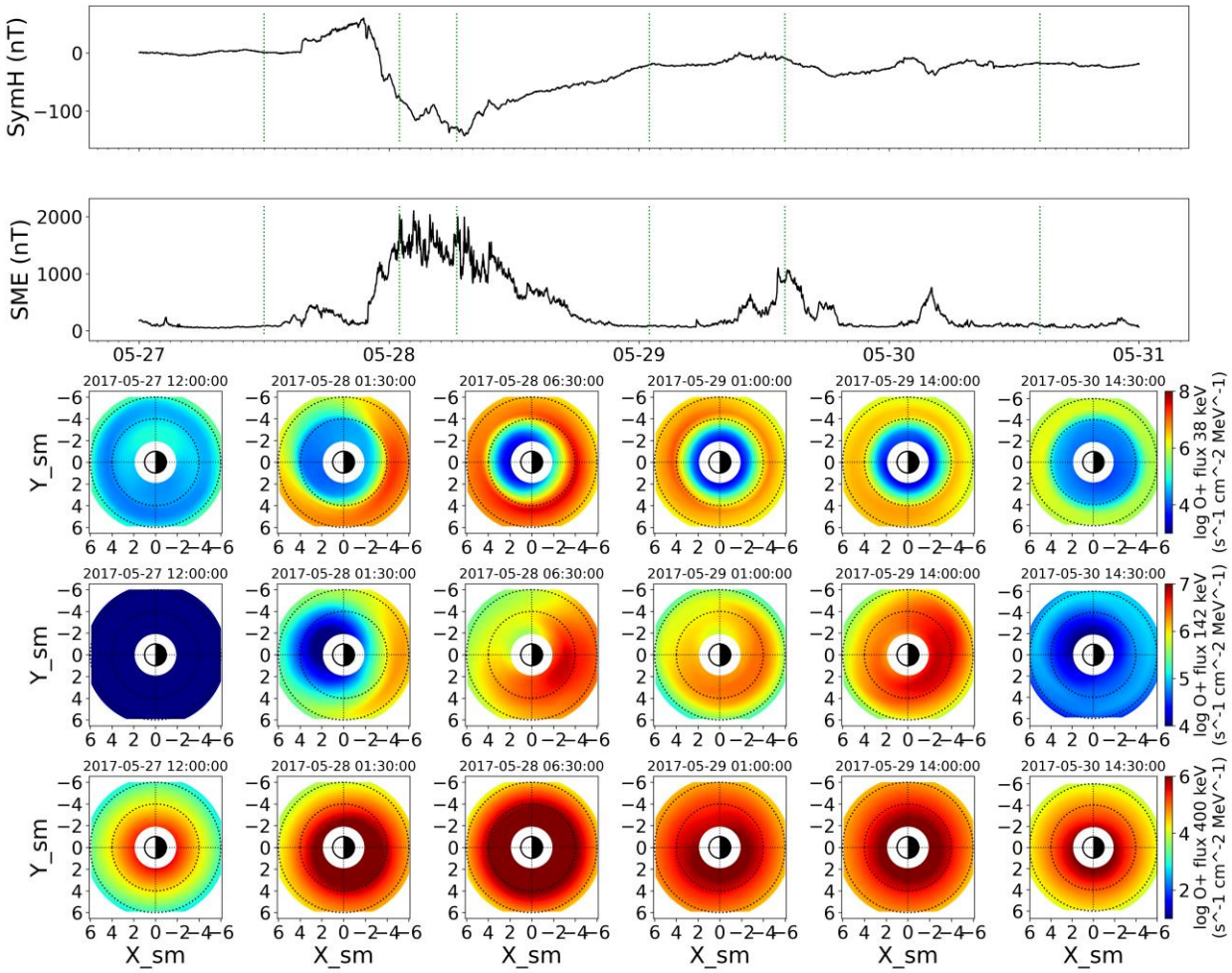

Figure 7: The Modeled global distribution of O+ flux spanning from 27 May to 30 May 2017. (a) The Sym-H index. (b) The SME index. (c-h) Global distributions of 38 keV O+ fluxes at six moments representing the pre-storm phase, the early main phase, the late main phase, the early recovery phase, the late recovery phase, and the post-storm time, respectively. (i-n) The variation of global distribution of 142 keV O+ flux, and (o-t), that of the 400 keV O+ flux at the same timestamps as above.

5 Conclusions

This study described the construction of a global, time-varying model of the ring current oxygen ions at a range of energies spanning the lower boundary to the upper energy boundary of the ring current ions, utilizing the ANN technique and trained on data measured on the Van Allen Probes. This model is driven by the time histories of the geomagnetic and solar indices, and does not require any initial and/or boundary conditions. Hence, this model is capable of reconstructing the oxygen fluxes for periods outside of the Van Allen Probe era (2012-2019) as long as geomagnetic index information is available. Although this paper only shows the O+ model at representative energies, we have established the ANN O+ flux model at a range of energies spanning from 38 keV to 870 keV based on the HOPE and RBSPICE measurements.

We summarize the model performance below:

(1) The model performance on the test set, exhibits a robust coefficient of determination ($R > 0.8$). This impressive result underscores the model's high precision in predicting out-of-sample data.

(2) The model successfully captures the results of various intricate processes involving the enhancement and loss of oxygen ions during geomagnetic storms throughout the year 2017.

(3) In a specific test case involving the geomagnetic storm of May 2017, the model excels in reconstructing the dynamic global variations in the fluxes of 38, 142, and 400 keV oxygen ions. It accurately predicts the spatiotemporal flux variations that – we believe (as a result of our physical understanding) - come about as a result of injection of ions from the plasma sheet and the subsequent enhancement on the pre-midnight side for 38 and 142 keV oxygen ions.

Oxygen ions constitute a significant component of the storm-time ring current, they are closely related to subsequent space weather events, and are particularly observed during large geomagnetic storms. The study of oxygen ions within the ring current is pivotal for advancing our comprehension of space weather and its repercussions on various technological systems. Modeling the enhancement and loss processes of oxygen ions serves as a key aspect in unraveling the dynamic characteristics of the inner magnetosphere. The application of ANN techniques in modeling oxygen ion flux populations offers a novel and versatile approach. This methodology can be readily extended to other ion species and energy channels, thus broadening its applicability in the realm of space physics and space weather research.

Acknowledgments

The study was supported by NSFC research Grant 42274200 and 41974191.

Open Research

The RBSPICE data is publically available at https://rbspice.ftecs.com/Data.html. The HOPE data is publically availably at https://rbsp-ect.newmexicoconsortium.org/. The 1-min resolution Sym/Asy indices used in this study are from Coordinated Data Analysis Web (CDAWeb) (https://cdaweb.gsfc.nasa.gov), and SME is from the SuperMAG (https://supermag.jhuapl.edu/) . The 1-day resolution F10.7 used in this study is from CelesTrak (https://celestrak.org/).

References

Baumjohann, Wolfgang. (1993). The near-Earth plasma sheet: An AMPTE/IRM perspective. *Space Science Reviews*, *64*(1–2), 141–163.

Baumjohann, W., & Treumann, R. A. (1996). *Basic Plasma Space Physics*. Imperial College Press, London.

Bortnik, J., Li, W., Thorne, R. M., & Angelopoulos, V. (2016). A unified approach to inner magnetospheric state prediction. *Journal of Geophysical Research: Space Physics*, *121*(3), 2423–2430.

Bortnik, J., Chu, X., Ma, Q., Li, W., Zhang, X., Thorne, R. M., … Others. (2018). Artificial neural networks for determining magnetospheric conditions. In *Machine learning techniques for space weather* (pp. 279–300). Elsevier.

Chappell, C. R., Moore, T. E., & Waite, J. H., Jr. (1987). The ionosphere as a fully adequate source of plasma for the Earth's magnetosphere. *Journal of Geophysical Research: Space Physics*, *92*(A6), 5896–5910.

Chappell, C. R., Giles, B. L., Moore, T. E., Delcourt, D. C., Craven, P. D., & Chandler, M. O. (2000). The adequacy of the ionospheric source in supplying magnetospheric plasma. *Journal of Atmospheric and Solar-Terrestrial Physics*, *62*(6), 421–436.

Chappell, C. R., Huddleston, M. M., Moore, T. E., Giles, B. L., & Delcourt, D. C. (2008). Observations of the warm plasma cloak and an explanation of its formation in the magnetosphere. *Journal of Geophysical Research: Space Physics*, *113*(A9).

Chen, A., Yue, C., Chen, H., Zong, Q., Fu, S., Wang, Y., & Ren, J. (2020). Ring current decay during geomagnetic storm recovery phase: comparison between rbsp observations and theoretical modeling. Journal of Geophysical Research: Space Physics, 125, e2020JA028500. https://doi.org/10.1029/2020JA028500

Chu, X., Bortnik, J., Li, W., Ma, Q., Denton, R., Yue, C., … Others. (2017). A neural network model of three-dimensional dynamic electron density in the inner magnetosphere. *Journal of Geophysical Research: Space Physics*, *122*(9), 9183–9197.

Chu, X. N., Bortnik, J., Li, W., Ma, Q., Angelopoulos, V., & Thorne, R. M. (2017). Erosion and refilling of the plasmasphere during a geomagnetic storm modeled by a neural network. *Journal of Geophysical Research: Space Physics*, *122*(7), 7118–7129.

Chu, Xiangning, Ma, D., Bortnik, J., Tobiska, W. K., Cruz, A., Bouwer, S. D., … Others. (2021). Relativistic electron model in the outer radiation belt using a neural network approach. *Space Weather*, *19*(12), e2021SW002808.

Claudepierre, S. G., Chen, M. W., Roeder, J. L., & Fennell, J. F. (2016). An empirical model of ion plasma in the inner magnetosphere derived from CRRES/MICS measurements. *Journal of Geophysical Research: Space Physics*, *121*(12), 11–780.

Claudepierre, Seth G., & O'Brien, T. P. (2020). Specifying high-altitude electrons using low-altitude leo systems: The shells model. *Space Weather*, *18*(3), e2019SW002402.

Daglis, I. A., Sarris, E. T., & Wilken, B. (1993). AMPTE/CCE CHEM observations of the energetic ion population at geosynchronous altitudes. *Annales Geophysicae*, *11*, 685–696.

Daglis, I. A. (1997). The role of magnetosphere-ionosphere coupling in magnetic storm dynamics. *Washington DC American Geophysical Union Geophysical Monograph Series*, *98*, 107–116.

Daglis, I. A., Thorne, R. M., Baumjohann, W., & Orsini, S. (1999). The terrestrial ring current: Origin, formation, and decay. *Reviews of Geophysics*, *37*(4), 407–438.

De Michelis, P., Daglis, I. A., & Consolini, G. (1997). Average terrestrial ring current derived from AMPTE/CCE-CHEM measurements. *Journal of Geophysical Research: Space Physics*, *102*(A7), 14103–14111.

Delcourt, D. C., Moore, T. E., Sauvaud, J. A., & Chappell, C. R. (1992). Nonadiabatic transport features in the outer cusp region. *Journal of Geophysical Research: Space Physics*, *97*(A11), 16833–16842.

Donovan, E. F., Jackel, B., Strangeway, R., & Klumpar, D. (2003). Energy dependence of the latitude of the 1--25 KeV ion isotropy boundary. *Sodankylä Geophysical Observatory Publications*, *92*, 11–14.

Fu, H., Yue, C., Zong, Q.-G., Zhou, X.Z., Yu, Y., Li, Y., et al. (2023). Substorm influences on plasma pressure and current densities inside the geosynchronous orbit. Journal of Geophysical Research: Space Physics, 128, e2022JA031099. https://doi. org/10.1029/2022JA031099

Funsten, H. O., Skoug, R. M., Guthrie, A. A., MacDonald, E. A., Baldonado, J. R., Harper, R. W., et al. (2013). Helium, oxygen, proton, and electron (HOPE) mass spectrometer for the radiation belt storm probes mission. Space Science Reviews, 179(1 ‐ 4), 423–484. https://doi. org/10.1007/s11214 ‐ 013 ‐ 9968 ‐ 7

Gkioulidou, M., Ohtani, S., Ukhorskiy, A. Y., Mitchell, D. G., Takahashi, K., Spence, H. E., … Barnes, R. J. (2019). Low-energy (< keV) O+ ion outflow directly into the inner magnetosphere: Van Allen Probes observations. *Journal of Geophysical Research: Space Physics*, *124*(1), 405–419.

Guo, Y., Ni, B., Fu, S., Wang, D., Shprits, Y. Y., Zhelavskaya, I. S., … Guo, D. (2022). Identification of controlling geomagnetic and solar wind factors for magnetospheric chorus intensity using feature selection techniques. *Journal of Geophysical Research: Space Physics*, *127*(1), e2021JA029926.

Huddleston, M. M., Chappell, C. R., Delcourt, D. C., Moore, T. E., Giles, B. L., & Chandler, M. O. (2005). An examination of the process and magnitude of ionospheric plasma supply to the magnetosphere. *Journal of Geophysical Research: Space Physics*, *110*(A12).

Jordanova, V. K., Kozyra, J. U., Khazanov, G. V., Nagy, A. F., Rasmussen, C. E., & Fok, M.-C. (1994). A bounce-averaged kinetic model of the ring current ion population. *Geophysical Research Letters*, *21*(25), 2785–2788.

Jordanova, V. K., Kozyra, J. U., Nagy, A. F., & Khazanov, G. V. (1997). Kinetic model of the ring current-atmosphere interactions. *Journal of Geophysical Research: Space Physics*, *102*(A7), 14279–14291.

Jordanova, Vania K. (2007). Modeling geomagnetic storm dynamics: New results and challenges. *Journal of Atmospheric and Solar-Terrestrial Physics*, *69*(1–2), 56–66.

Keesee, A. M., Buzulukova, N., Goldstein, J., McComas, D. J., Scime, E. E., Spence, H., … Tallaksen, K. (2011). Remote observations of ion temperatures in the quiet time magnetosphere. *Geophysical Research Letters*, *38*(3).

Keika, K., Kistler, L. M., & Brandt, P. C. (2013). Energization of O+ ions in the Earth's inner magnetosphere and the effects on ring current buildup: A review of previous observations and possible mechanisms. *Journal of Geophysical Research: Space Physics*, *118*(7), 4441–4464.

Keika, K., Seki, K., Nosé, M., Machida, S., Miyoshi, Y., Lanzerotti, L. J., … Others. (2016). Storm time impulsive enhancements of energetic oxygen due to adiabatic acceleration of preexisting warm oxygen in the inner magnetosphere. *Journal of Geophysical Research: Space Physics*, *121*(8), 7739–7752.

Keika, K., Kasahara, S., Yokota, S., Hoshino, M., Seki, K., Nosé, M., … Shinohara, I. (2018). Ion energies dominating energy density in the inner magnetosphere: Spatial distributions and composition, observed by Arase/MEP-i. *Geophysical Research Letters*, *45*(22), 12–153.

Kennel, C. F., & Petschek, H. E. (1966). Limit on stably trapped particle fluxes. *Journal of Geophysical Research*, *71*(1), 1–28.

Kivelson, M. G., & Spence, H. E. (1988). On the possibility of quasi-static convection in the quiet magnetotail. *Geophysical Research Letters*, *15*(13), 1541–1544.

Kistler, L. M., & Mouikis, C. G. (2016). The inner magnetosphere ion composition and local time distribution over a solar cycle. *Journal of Geophysical Research: Space Physics*, *121*(3), 2009–2032.

Kronberg, E. A., Ashour-Abdalla, M., Dandouras, I., Delcourt, D. C., Grigorenko, E. E., Kistler, L. M., … Others. (2014). Circulation of heavy ions and their dynamical effects in the magnetosphere: Recent observations and models. *Space Science Reviews*, *184*, 173–235.

Landis, D. A., Saikin, A. A., Zhelavskaya, I., Drozdov, A. Y., Aseev, N., Shprits, Y. Y., … Smirnov, A. G. (2022). NARX neural network derivations of the outer boundary radiation belt electron flux. *Space Weather*, *20*(5), e2021SW002774.

Li, J., Bortnik, J., Chu, X., Ma, D., Tian, S., Wang, C.-P., … Lanzerotti, L. J. (2023). Modeling ring current proton fluxes using artificial neural network and Van Allen Probe measurements. *Space Weather*, *21*(5), e2022SW003257.

Liang, J., Donovan, E., Ni, B., Yue, C., Jiang, F., & Angelopoulos, V. (2014). On an energy-latitude dispersion pattern of ion precipitation potentially associated with magnetospheric EMIC waves. *Journal of Geophysical Research: Space Physics*, *119*(10), 8137–8160.

Ma, D., Chu, X., Bortnik, J., Claudepierre, S. G., Tobiska, W. K., Cruz, A., … Blake, J. B. (2022). Modeling the dynamic variability of sub-relativistic outer radiation belt electron fluxes using machine learning. *Space Weather*, *20*(8), e2022SW003079.

Meredith, N. P., Thorne, R. M., Horne, R. B., Summers, D., Fraser, B. J., & Anderson, R. R. (2003). Statistical analysis of relativistic electron energies for cyclotron resonance with EMIC waves observed on CRRES. *Journal of Geophysical Research: Space Physics*, *108*(A6).

Milillo, A., Orsini, S., & Daglis, I. A. (2001). Empirical model of proton fluxes in the equatorial inner magnetosphere: Development. *Journal of Geophysical Research: Space Physics*, *106*(A11), 25713–25729.

Mitchell, D. G., Lanzerotti, L. J., Kim, C. K., Stokes, M., Ho, G., Cooper, S., et al. (2013). Radiation belt storm probes ion composition experiment (RBSPICE). Space Science Reviews, 179(1 ‐ 4), 263–308. https://doi.org/10.1007/s11214 ‐ 013 ‐ 9965 ‐ x

Ramachandran, P., Zoph, B., & Le, Q. V. (2017). Searching for activation functions. *arXiv Preprint arXiv:1710. 05941*.

Roeder, J. L., Chen, M. W., Fennell, J. F., & Friedel, R. (2005). Empirical models of the low-energy plasma in the inner magnetosphere. *Space Weather*, *3*(12).

Rumelhart, D. E., Hinton, G. E., & Williams, R. J. (1986). Learning Representations by Back-Propagating Errors. Nature, 323, 533-536. https://doi.org/10.1038/323533a0

Sergeev, V. A., & Tsyganenko, N. A. (1982). Energetic particle losses and trapping boundaries as deduced from calculations with a realistic magnetic field model. *Planetary and Space Science*, *30*(10), 999–1006.

Sergeev, V. A., Sazhina, E. M., Tsyganenko, N. A., Lundblad, J. Å., & Søraas, F. (1983). Pitch-angle scattering of energetic protons in the magnetotail current sheet as the dominant source of their isotropic precipitation into the nightside ionosphere. *Planetary and Space Science*, *31*(10), 1147–1155.

Sergeev, V. A., Malkov, M., & Mursula, K. (1993). Testing the isotropic boundary algorithm method to evaluate the magnetic field configuration in the tail. *Journal of Geophysical Research: Space Physics*, *98*(A5), 7609–7620.

Sheldon, R. B., Spence, H. E., & Fennell, J. F. (1998). Observation of the 40 keV field-aligned ion beams. *Geophysical Research Letters*, *25*(10), 1617–1620.

Smith, P. H., Bewtra, N. K., & Hoffman, R. A. (1981). Inference of the ring current ion composition by means of charge exchange decay. *Journal of Geophysical Research: Space Physics*, *86*(A5), 3470–3480.

Spence, H. E., & Kivelson, M. G. (1990). The variation of the plasma sheet polytropic index along the midnight meridian in a finite width magnetotail. *Geophysical Research Letters*, *17*(5), 591–594.

509 Spence, H. E., & Kivelson, M. G. (1993). Contributions of the low-latitude boundary layer to the finite width
510 magnetotail convection model. *Journal of Geophysical Research: Space Physics*, *98*(A9), 15487–
511 15496.
512 Toffoletto, F., Sazykin, S., Spiro, R., & Wolf, R. (2003). Inner magnetospheric modeling with the Rice
513 Convection Model. *Space Science Reviews*, *107*, 175–196.
514 Williams, D. J. (1987). Ring current and radiation belts. *Reviews of Geophysics*, *25*(3), 570–578.
515 Yang, B., Zong, Q.-G., Fu, S. Y., Li, X., Korth, A., Fu, H. S., … Reme, H. (2011). The role of ULF waves
516 interacting with oxygen ions at the outer ring current during storm times. *Journal of Geophysical*
517 *Research: Space Physics*, *116*(A1).
518 Yue, C., J. Bortnik, L. Chen, Q. Ma, R. M. Thorne, G. D. Reeves, and H. E. Spence (2017), Transitional
519 behavior of different energy protons based on Van Allen Probes observations, Geophysical Research
520 Letters, 44, doi:10.1002/2016GL071324.
521 Yue, C., Wang, C.-P., Lyons, L., Liang, J., Donovan, E. F., Zaharia, S. G., & Henderson, M. (2014). Current
522 sheet scattering and ion isotropic boundary under 3-D empirical force-balanced magnetic
523 field. *Journal of Geophysical Research: Space Physics*, *119*(10), 8202–8211.
524 Yue, C., Bortnik, J., Li, W., Ma, Q., Gkioulidou, M., Reeves, G. D., … Others. (2018). The composition of
525 plasma inside geostationary orbit based on Van Allen Probes observations. *Journal of Geophysical*
526 *Research: Space Physics*, *123*(8), 6478–6493.
527 Yue, C., Bortnik, J., Li, W., Ma, Q., Wang, C.-P., Thorne, R. M., … Others. (2019). Oxygen ion dynamics in
528 the Earth's ring current: Van Allen Probes observations. *Journal of Geophysical Research: Space*
529 *Physics*, *124*(10), 7786–7798.
530 Yue, C. , Bortnik, J., Zou, S., Nishimura, Y., Foster, J. C., Coppeans, T., et al. (2020). Episodic Occurrence of
531 Field‐Aligned Energetic Ions on the Dayside. Geophysical Research Letters, 47, e2019GL086384.
532 https://doi.org/ 10.1029/2019GL086384
533 Zhelavskaya, I. S., Shprits, Y. Y., & Spasojević, M. (2017). Empirical modeling of the plasmasphere dynamics
534 using neural networks. *Journal of Geophysical Research: Space Physics*, *122*(11), 11–227.

Zong, Q.-G., Wang, Y. F., Zhang, H., Fu, S. Y., Zhang, H., Wang, C. R., … Vogiatzis, I. (2012). Fast acceleration of inner magnetospheric hydrogen and oxygen ions by shock induced ULF waves. *Journal of Geophysical Research: Space Physics*, *117*(A11).

Zhou, X.-Z., Ge, Y. S., Angelopoulos, V., Runov, A., Liang, J., Xing, X., … Zong, Q.-G. (2012). Dipolarization fronts and associated auroral activities: 2. Acceleration of ions and their subsequent behavior. *Journal of Geophysical Research: Space Physics*, *117*(A10).